

1 Time-frequency domain characteristics analysis of a hydro-turbine governor system 2 considering vortex rope excitation

3 Liuwei Lei^{a,b,c,#}, Feng Li^{b,c,#}, Beibei Xu^{*,a,b,c,d}, Mònica Egusquiza^e, Xingqi Luo^a, Junzhi Zhang^d, Eduard
4 Egusquiza^e, Diyi Chen^{b,c}, Wei Jiang^{b,c}, Edoardo Patelli^f

5
6 *^aState Key Laboratory of Eco-hydraulics in Northwest Arid Region, Xi'an University of Technology, Xi'an,
7 710048, Shaanxi, P.R. China*

8 *^bKey Laboratory of Agricultural Soil and Water Engineering in Arid and Semiarid Areas, Ministry of
9 Education, Northwest A & F University, Shaanxi Yangling 712100, P. R. China*

10 *^cInstitute of Water Resources and Hydropower Research, Northwest A&F University, Shaanxi Yangling
11 712100, P. R. China*

12 *^dPowerchina Northwest Engineering Corporation Limited, Limited, Xi'an, 710065, P.R. China*

13 *^eCenter for Industrial Diagnostics and Fluid Dynamics (CDIF), Polytechnic University of Catalonia
14 (UPC), Av. Diagonal, 647, ETSEIB, 08028 Barcelona, Spain*

15 *^fDepartment of civil and environmental engineering, University of Strathclyde, U.K.*

16
17 **#These authors contribute equally to this paper.**

18 ***Corresponding author: Beibei Xu**

19 **Mailing Address:** Institute of Water Resources and Hydropower Research, Northwest A&F University,
20 Shaanxi Yangling 712100, China

21 **Telephones:** 086-187-0080-9631

22 **E-mail:** xubeibei0413@163.com

23
24 **Abstract:** Understanding and simulating the dynamic characteristics of the hydro-turbine governor
25 system is essential to guarantee the safety of the hydro-power systems. This study proposes a modification
26 method of the water head at the draft tube inlet, which is to discretize the draft tube and introduce the
27 excitation term of the vortex rope. The proposed approach is applied for the modeling of the hydro-turbine
28 governor system. The proposed model (Model I) is verified by means of a comparison with a second
29 model (Model II) of the hydro-turbine governor system model without considering the vortex rope and
30 verified against the experimental data during the load reduction. The model developed is accurate
31 providing errors of the water head, inlet water head and flow of the hydro-turbine for Model I are within
32 $\pm 3.3\%$, $\pm 2\%$ and $\pm 5\%$, respectively. The proposed model overcomes the limitations of Model II in the
33 time-domain and frequency-domain since that only provides the average pressure at the draft tube, which
34 do not reflect the pressure fluctuation and energy fluctuation. Instead the proposed model allows to
35 capture and model the energy fluctuation during the load reduction as shown in the experimental results.
36 The proposed model promotes the development of the hydro-turbine governor system model.

37 **Keywords:** Vortex rope; Hydro-turbine governor system; Modeling method; Francis turbine; Dynamic
38 characteristics analysis.

39 1.Introduction

40 Hydropower is the excellent renewable energy with many advantages [1], such as no fuel, low cost,
41 no environmental pollution and flexible operation. On the one hand, hydropower reduces the uncertainty
42 of the power output and ensures the safe and stable operation of the power grid through the flexible
43 operation. On the other hand, hydropower reduces the greenhouse gas emissions by replacing the fossil
44 energy, helping to achieve the goal of "carbon neutral". Therefore, hydropower plays an essential role in
45 optimizing the power grid structure and achieving the sustainability goals [2].

46 Furthermore, the function of the hydroelectric generating unit has changed from "energy supply" to
47 "energy regulation" under the background of the energy reform [3]. Thus, the unit operation under the
48 partial load becomes more and more important where the draft tube produces the vortex rope [4-5], which
49 in turn causes the high intensity and low frequency pressure fluctuations [6], leading to the fluctuation of
50 the hydro-turbine water head [7]. This fluctuation threatens the safety of the hydro-turbine governor
51 system and the stability of the power grid frequency [8]. Therefore, more attention needs to be paid to the
52 stability problem of the hydro-turbine governor system caused by the vortex rope in the draft tube.

53 The pressure fluctuation caused by the vortex rope, can be study using the theoretical methods [9],
54 or performing the experimental tests [10] or via the numerical simulation [11]. The theoretical analysis
55 allows to deduce the law reflecting the internal flow of the draft tube by using the logical relationship
56 [12]. Nishi et al. [13] used the static vortex rope model to predict the precession frequency of the vortex
57 rope in the draft tube, but the universality of this method needs to be further verified. On this basis, Wu
58 et al. [14] deduced the relationship between the hydro-turbine operating conditions and the pressure
59 fluctuation in the draft tube and proposed a calculation formula of the velocity rotation component, which
60 opened a new idea for the study of the vortex rope formation mechanism. However, the flow
61 characteristics of the vortex rope are complex and the simplification introduced by the analytical
62 approaches limit their applicability.

63 The experimental research requires the availability and access to the real machines and perform the
64 experiments. The cost of such experiments is generally very high and the operation is difficult [15].
65 Kirschner et al. [16] studied the relationship between the pressure fluctuation frequency measured at the
66 draft tube wall and the movement of the vortex rope by using the particle image velocimetry. The results
67 showed that the low frequency pressure fluctuation is correlating with the vortex rope movement. In [17],
68 Arthur et al. proved that the impact of both the speed and discharge factors on the precession frequency
69 and the system natural frequency can be represented only by the swirl number through a reduced scale
70 physical model of a Francis hydro-turbine. Qiao et al. [18] discovered that the draft tube pressure
71 fluctuation affects the swing of the unit and identified the hydraulic instability factors causing the impact
72 by conducting a full range variable load test on a 200MW Francis hydro-turbine, which provided a
73 guarantee for the safe operation of the unit. Because of the associated costs, the experimental research is
74 rarely and often used together with the numerical simulations.

75 The numerical experiments are used to overcome the limitation of the theoretical and experimental
76 approaches where the mathematical models are solved numerically by the computer program. Although
77 the accuracy and reliability of the numerical simulation might be inferior to the experimental research, it
78 is the low-cost approach and easy to operate [19-20]. Liu et al. [21] simulated the dynamic characteristics

79 of the pump turbine in the transient process based on the dynamic grid method, and obtained that the inlet
80 flow from the draft tube to the runner had the greatest influence on the pressure fluctuation under the
81 condition of the reverse flow. Nahale et al. [22] used the transient numerical simulation method to study
82 the dynamic characteristics of the vortex rope during the load change process identifying the four different
83 flow states of the vortex rope. In [23], Alexis et al. used a three-dimensional simulation model, and found
84 that the low-frequency disturbances, as instabilities taking source from the fluid structure itself, can
85 override strong flow gradients and exert a higher backward influence farther than the high-frequency
86 perturbations. Simon et al. [24] proposed to use the optimal control theory to control the vortex rope,
87 which was verified by the numerical simulation. This method shrinks the vortex rope to the center line of
88 the draft tube and suppresses the pressure fluctuation in the draft tube. Sébastien et al [25] established a
89 one-dimensional draft tube model based on the flow equation and the momentum equation, which
90 introduced the convective terms in the momentum equation and combined with the divergent geometry
91 of the draft tube. The model enhanced the applicability of the one-dimensional draft tube model. The
92 above research analyzed the dynamic characteristics of the vortex rope in detail and found that the
93 pressure fluctuation of the draft tube affects the stability of the hydro-turbine governor system, but did
94 not consider the vortex rope in detail from the perspective of the hydro-turbine governor system. Because
95 the vortex rope affects the hydro-turbine governor system through the water head, further research is still
96 needed to study the modification of the water head calculation method at the inlet of the draft tube and its
97 application to the hydro-turbine governor system model.

98 From the above review, even though the hydro-turbine governor system is affected by the vortex
99 rope in the draft tube, this is seldom investigated. Doing so could bring a different perspective and expand
100 the current understanding. Studies on the model of the hydro-turbine governor system are relatively
101 simple and some characteristics of the pressure fluctuation caused by the vortex rope are not captured.
102 Therefore, the main objectives of this study are: (i) To establish the relationship between the hydro-turbine
103 governor system and the vortex rope in the draft tube, (ii) to analyze the time-frequency domain
104 characteristic information of the vortex rope excitation, (iii) to analyze the influence of the guide vane
105 closing time on the draft tube pressure fluctuation during the load reduction.

106 This paper focuses on improving the calculation accuracy of the water head at the draft tube in the
107 hydro-turbine governor system. Therefore, this work proposes the following three main novel aspects:

- 108 •The vortex rope excitation is innovatively introduced into the hydro-turbine governor system
109 model;
- 110 •The correctness of the proposed model is verified in the time domain and the frequency domain
111 combined with the experimental data;
- 112 •The optimum ΔT is found by analyzing the relationship between different ΔT and the characteristics
113 of the draft tube pressure fluctuation.

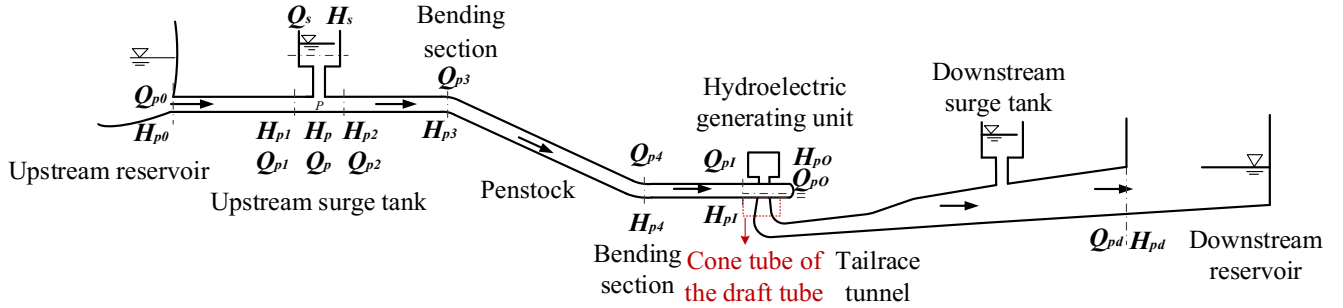
114 This paper is structured as following. In Section 2, the hydro-turbine governor system model
115 considering the vortex rope is established. In Section 3, the proposed model is analyzed and verified in
116 the time domain and the frequency domain, respectively, by comparing with the experimental data and
117 the previous model. Finally, the conclusions are given in Section 4.

Nomenclature		R_λ	Resistance
<i>Abbreviations</i>		R_d	Negative impedance
HGS	Hydroelectric Generating System	μ	Expansion viscosity
MOC	Method of characteristics	R_μ	Resistance
TPS	Thin Plate Splines	C_c	Capacitance
BEP	Best efficiency point	δx	Length of each section of the draft tube
PL	Part load	λ	Coefficient of local head loss
VMD	Variational mode decomposition	K_x	Geometric divergence rate
<i>Parameters</i>		μ''	Expansion viscosity
Δt	Time step	D_I	Runner diameter
x	Length of the pipe	<i>Variables</i>	
D	Inner diameter of the pipe	ΔT	Guide vane closing time
g	Gravitational acceleration	Q	Flow rate
f	Darcy-Weisbach coefficient of friction	H	Water head
α	Angle between the pipe and water level	v	Flow velocity
a	Pressure wave velocity	t	Time
A	Section area	n_0	Hydro-turbine speed
R_S	Restricted coefficient of the surge tank	n_{11}	Unit speed
$A_{\omega S}$	Area of the impedance hole	Q_t	Hydro-turbine flow
A_S	Area of the surge tank	Q_{11}	Unit flow
ξ	Coefficient of the local head loss	y	Guide vane opening
J	Convection term defines	M_t	Hydro-turbine torque
L	Inductance	M_{11}	Unit torque

118

119 **2. Mathematic modeling**

120 The structure of the Hydroelectric Generating System (HGS) is shown in Fig. 1, which is composed
 121 of the upstream reservoir, headrace tunnel, upstream surge tank, penstock, hydroelectric generating unit,
 122 tailrace tunnel, downstream surge tank and downstream reservoir. The meanings of the parameters in Fig.
 123 1 are as follows. Parameters Q_{p0} and H_{p0} are the flow rate and water head at the head of the headrace
 124 tunnel; parameters H_s and Q_s are the water level in the surge tank and the flow rate from the impedance
 125 hole P to the surge tank; parameters H_{p1} and Q_{p1} are the water head and flow rate at the end of the headrace
 126 tunnel; parameters H_{p2} and Q_{p2} are the water head and flow rate at the head of the penstock; parameters
 127 H_p and Q_p are the water head and flow rate at the bottom of the surge tank; parameters H_{p3} , H_{p4} , Q_{p3} , and
 128 Q_{p4} are the water head and flow rate at the bending section; parameters H_{p1} , H_{pO} , Q_{p1} , and Q_{pO} are the
 129 water head and flow rate at the inlet and outlet of the hydro-turbine; parameters Q_{pd} and H_{pd} are the flow
 130 rate and water head at the end of the tailrace tunnel. This section proposes a nonlinear mathematical model
 131 of the hydro-turbine governor system with the cone tube of the draft tube considering the influence of the
 132 vortex rope according to the method of characteristics (MOC) and the equivalent circuit method, which
 133 is suitable for the simulation of the transition process of HGS.



134
135 **Fig. 1** The layout of the Hydroelectric Generating System.
136

137 2.1 The headrace and penstock model

138 The pressure pipe model describes the dynamic behavior of the pressure unsteady flow. The basic
 139 equations of the transient flow calculation for the pressure pipe are the continuum equation and movement
 140 equation, which are [26-27]

$$\begin{cases} L_1: \frac{\partial v}{\partial t} + v \frac{\partial v}{\partial x} + g \frac{\partial H}{\partial x} + \frac{fv|v|}{2D} = 0 \\ L_2: \frac{\partial H}{\partial t} + v \frac{\partial H}{\partial x} + \frac{a^2}{g} \frac{\partial v}{\partial x} + v \sin \alpha = 0 \end{cases} \quad (1)$$

142 Where v is the flow velocity; H is the water head of the pipeline; x is the length of the pipe; D is the inner
 143 diameter of the pipe; g is the gravitational acceleration; f is the Darcy-Weisbach coefficient of friction; α
 144 is the angle between the pipe and water level; t is time; a is the pressure wave velocity.

145 The partial differential equations of the transient flow in the pressurized pipes are solved by MOC,
 146 which uses an undetermined coefficient λ to connect and linearly combine.

$$147 \quad L = L_1 + \lambda L_2 \quad (2)$$

148 Where L_1 and L_2 are the first and second equation of Eq. (1), respectively.

149 From Eqs. (1) and (2):

$$150 \quad \left[\frac{\partial v}{\partial t} + \left(v + \lambda \frac{a^2}{g} \right) \frac{\partial v}{\partial x} \right] + \lambda \left[\frac{\partial H}{\partial t} + \left(v + \frac{g}{\lambda} \right) \frac{\partial H}{\partial x} \right] + \lambda v \sin \alpha + \frac{fv|v|}{2D} = 0. \quad (3)$$

151 Letting $H=H(x,t)$ and $v=v(x,t)$ be the solution of the Eq. (3), so its total differential is written as:

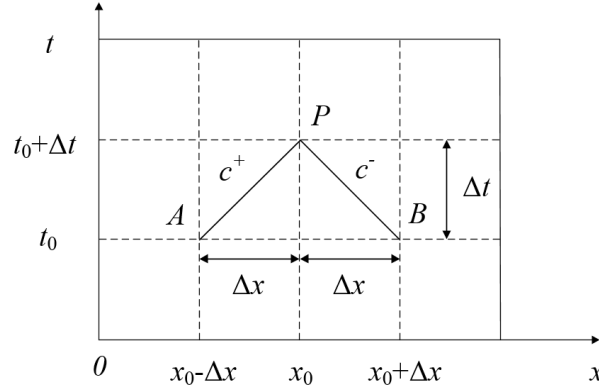
$$152 \quad \begin{cases} \frac{dv}{dt} = \frac{\partial v}{\partial t} + \frac{\partial v}{\partial x} \frac{dx}{dt} \\ \frac{dH}{dt} = \frac{\partial H}{\partial t} + \frac{\partial H}{\partial x} \frac{dx}{dt} \end{cases}. \quad (4)$$

153 The characteristic line equation is obtained by taking $\lambda=\pm g/a$ and combing Eqs. (3) and (4).

$$154 \quad \begin{cases} c^+ : \frac{dx}{dt} = v + a \\ c^- : \frac{dx}{dt} = v - a \end{cases} \quad (5)$$

155 Along the direction of the characteristic line, the corresponding compatibility equation is obtained [28].

$$156 \quad \begin{cases} c^+ : \frac{dH}{dt} + \frac{a}{g} \frac{dv}{dt} + v \sin \alpha + \frac{a}{g} \frac{fv|v|}{2D} = 0 \\ c^- : -\frac{dH}{dt} + \frac{a}{g} \frac{dv}{dt} - v \sin \alpha + \frac{a}{g} \frac{fv|v|}{2D} = 0 \end{cases} \quad (6)$$



157
158 **Fig. 2** The characteristic mesh in the x - t plane

159
160 The characteristic mesh in the x - t plane is shown in Fig. 2 [26]. In the x - t plane, the characteristic
161 lines are taken as grids (Δt is the time step and Δx is the length of pipe). The partial different equation is
162 converted into the finite difference equation by the characteristic lines (i.e., Eq. (5)) and the corresponding
163 compatibility equation (i.e., Eq. (6)). From Fig. 2, the state of point P at time $t=t_0+\Delta t$ is calculated by the
164 state of two nodes A and B at time $t=t_0$ through Eq. (7), which is obtained from Eqs. (5) and (6).

$$\begin{cases}
c^+ : H_p = C_M - C_{aA} v_p \\
c^- : H_p = C_N + C_{aB} v_p \\
C_M = H_A + C_{aA} (v_A - \frac{fv_A |v_A|}{2D} \Delta t) - v_A \sin \alpha \Delta t \\
C_{aA} = \frac{a_A}{g} \\
C_N = H_B - C_{aB} (v_B - \frac{fv_B |v_B|}{2D} \Delta t) - v_B \sin \alpha \Delta t \\
C_{aB} = \frac{a_B}{g}
\end{cases} \quad (7)$$

166 Where H_P , H_A , and H_B are the water head of the point of P , A , and B , respectively; v_P , v_A , and v_B are the
167 flow velocity of the point of P , A , and B , respectively; Δt is the time interval; a_A and a_B are the pressure
168 wave velocity of the point of A and B ; C_M , C_N , C_{aA} , and C_{aB} are the intermediate variables. By simplifying
169 the Eq. (7), the calculation formula of P point parameters is shown in Eq. (8).

$$\begin{cases}
v_p = \frac{C_M - C_N}{C_{aA} + C_{aB}} \\
H_p = C_M - C_{aA} \frac{C_M - C_N}{C_{aA} + C_{aB}}
\end{cases} \quad (8)$$

171

172 2.2 Boundary conditions

173 The boundary conditions are essential in the calculation of the flow rate and the water head in the
174 water diversion system by using MOC. The following boundary conditions are used in this study:

175

176 (1) Upstream reservoir

177 The upstream reservoir is the upper boundary of the water diversion system, ignoring the influence
178 of the local head loss and wind waves at the inlet of the pipe on the water level, that is, the upstream
179 reservoir water level remains constant in the transient flow process. Therefore, the upstream reservoir
180 boundary condition is established [29]. The water head and the flow rate at the upstream boundary are
181 calculated by Eq. (9).

$$\begin{cases}
H_{p0} = H_0 = const \\
Q_{p0} = \frac{H_{p0} - C_N}{C_{aB}} A_{p0}
\end{cases} \quad (9)$$

183

184 Where H_0 is the upstream reservoir water level; $const$ represents the constant; A_{p0} is the section area at
185 the head of the headrace tunnel; Q_{p0} and H_{p0} are the flow rate and water head at the head of the headrace
186 tunnel.

187

188 (2) Surge tank

189 The type of the surge tank selected in this study is the impedance surge tank, which is composed by
190 the upstream P_1 and downstream P_2 sections of the surge tank, the section S in the surge chamber and the
191 pressure pipe section P at the position of the surge tank [30-31].

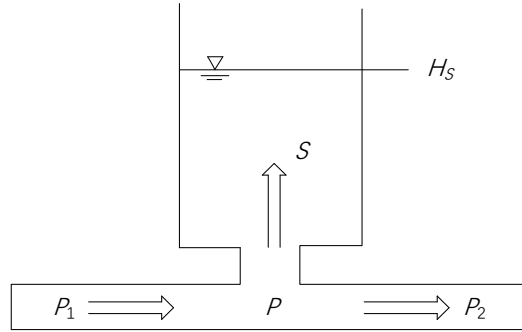


Fig. 3 The schematic diagram of the impedance surge tank. H_s is the water level of the surge tank; S represents the section of the surge tank; P represents the pressure pipe section at the position of the surge tank; P_1 and P_2 represent the upstream and downstream sections of the surge tank, respectively.

The upstream and downstream sections of the surge tank satisfy c^+ and c^- equation, which are shown in Eq. (10), respectively.

$$\begin{cases} H_{p_1} = C_M - C_{aA} v_{p_1} \\ H_{p_2} = C_N + C_{aB} v_{p_2} \end{cases} \quad (10)$$

Where v_{p_1} and H_{p_1} are the flow velocity and the water head at point P_1 ; v_{p_2} and H_{p_2} are the flow velocity and the water head at point P_2 . The water head and the flow rate in the surge tank meet Eq. (11).

$$\begin{cases} H_p = H_s + R_s \frac{Q_s |Q_s|}{A_{ws}^2} \\ H_s = H_{s_{t-\Delta t}} + \frac{(Q_s + Q_{s_{t-\Delta t}}) \Delta t}{2A_s} \\ H_{p_1} = H_{p_2} = H_p \\ Q_{p_1} = Q_{p_2} = Q_p + Q_s \end{cases} \quad (11)$$

Where A_{ws} is the area of the impedance hole; R_s is the restricted coefficient of the surge tank, $R_s=1/(2g\phi)$; ϕ generally changes in the internal $[0.6,0.8]$; A_s is the area of the surge tank; H_s is the water level in the surge tank; Q_s is the flow rate from the impedance hole P to the surge tank; H_p is the flow rate at the impedance hole P ; Q_{p_1} , Q_{p_2} , and Q_p are the flow rate of the point of P_1 , P_2 , and P . Combining Eqs. (10) and (11), the water head and flow rate at the surge tank are obtained.

(3) Bending section

The penstock contains two bending sections in this study. The boundary condition at the bending section is obtained as follows[32]. The front and rear sections of the bending section meet c^+ and c^- equation shown in Eq. (12), respectively.

$$\begin{cases} H_{p_{31}} = C_M - C_{aA} v_{p_{31}} \\ H_{p_{32}} = C_N + C_{aB} v_{p_{32}} \end{cases} \quad (12)$$

Where $H_{p_{31}}$ and $v_{p_{31}}$ are the water head and the flow velocity in front of the bending section; $H_{p_{32}}$ and $v_{p_{32}}$ are the water head and the flow velocity after the bending section.

216 The bending section also satisfies the flow and water head balance equation as shown in Eq. (13).

$$217 \quad \begin{cases} Q_{p31} = Q_{p32} \\ H_{p31} = H_{p32} + \xi \frac{v_{p32}^2}{2g} \end{cases} \quad (13)$$

218 Where ξ is the coefficient of the local head loss. Combining Eqs. (12) and (13), the water head and the
219 flow rate at the bending section are obtained.

220

221 (4) Hydro-turbine

222 The flow rate and torque for the hydro-turbine transition process are calculated by the hydro-turbine
223 characteristic curve, which is generally in part of the data through the interpolation or fitting method. Thin
224 Plate Splines (TPS) is a point-based nonlinear transformation method[33-34], which has the clear physical
225 significance. It describes the rigid transformation similar to the metal sheet. The interpolation problem is
226 simulated as the bending deformation of a thin metal plate under the constraint of point, and the
227 deformation energy is represented by an algebraic expression. Therefore, for the above problems, TPS
228 interpolation is used to calculate the hydro-turbine flow rate and torque.

229 The hydro-turbine flow rate at the inlet is approximately equal to the hydro-turbine flow rate. The
230 water head at the inlet and outlet satisfies c^+ and c^- equation, respectively. So, the hydro-turbine boundary
231 condition is established and the water head and flow rate at the inlet and outlet of the hydro-turbine are
232 calculated by Eq. (14).

$$233 \quad \begin{cases} H_{pl} = C_M - C_{aA} \frac{Q_{pl}}{A_{pl}} \\ H_{po} = C_N + C_{aB} \frac{Q_{po}}{A_{po}} \\ Q_{pl} = Q_{po} = Q_t \end{cases} \quad (14)$$

234 Where A_{pl} and A_{po} represent the pipe cross section area at the inlet and outlet of the hydro-turbine,
235 respectively; H_{pl} , H_{po} , Q_{pl} , and Q_{po} are the water head and flow rate at the inlet and outlet of the hydro-
236 turbine; Q_t is the hydro-turbine flow rate.

237

238 (5) Downstream reservoir

239 The flow velocity at the downstream reservoir is relatively small. Thus, the kinetic energy loss and
240 local head loss are ignored. The boundary condition of the downstream reservoir is established as shown
241 below[32]. Therefore, the water head and the flow rate at the downstream boundary are calculated by Eq.
242 (15).

$$243 \quad \begin{cases} H_{pd} = H_d = const \\ Q_{pd} = \frac{C_M - H_{pd}}{C_{aA}} A_{pd} \end{cases} \quad (15)$$

244 Where H_d is the downstream reservoir water level; A_{pd} is the section area at the end of the tailrace tunnel;
 245 Q_{pd} and H_{pd} are the flow rate and the water head at the end of the tailrace tunnel.

246

247 2.3 The cone tube of the draft tube model

248

249

250

251

252

253

254

255

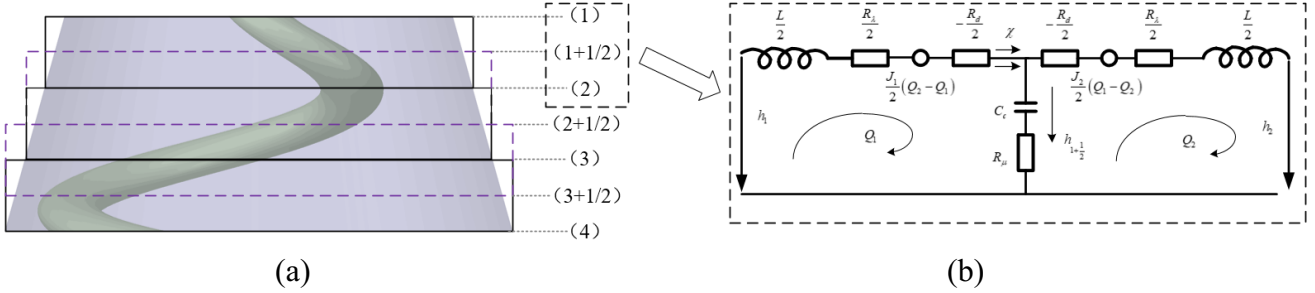
256

257

258

259

260



250 **Fig. 4** The Schematic diagram of the cone tube of the draft tube model (a) [35] and its equivalent circuit diagram (b).

252 Fig. 4(a) shows the schematic diagram of the cone tube of the draft tube according to [35]. As this
 253 part of the pipe is a geometric divergence tube, the cone model is equivalent to the electric circuit shown
 254 in Fig. 4(b). The equivalent electrical circuit has been obtained considering the continuity equation, the
 255 momentum equation and the convection term [25, 35]. The convection term defines J ; the fluid inertia
 256 represents the inductance L and the energy loss is modeled by the resistance R_λ , respectively. The effect
 257 of the pipe geometry on the pressure change (geometric dissipation) is equivalent to the negative
 258 impedance R_d ; the dissipation due to the expansion viscosity μ is equivalent to the resistance R_μ ; the
 259 cavitation flexibility, which is equivalent to the capacitance C_c , is used to express the effect of the
 260 divergent geometry on the damping. Therefore, the module models of the equivalent circuit are as follows:

261

$$\begin{cases} L = \frac{\delta x}{gA}, & R_\lambda = \frac{\lambda \delta x}{2gDA^2} Q, & R_d = \frac{\delta x K_x}{gA^3} Q \\ C_c = \frac{gAL_p}{a^2}, & J = \frac{Q}{gA^2}, & R_\mu = \frac{\mu''}{\rho g A \delta x} \end{cases} \quad (16)$$

262

263

264

265

266

Where δx is the length of each section of the draft tube; g is the acceleration of gravity; A is the cross-sectional area of the section; λ is the coefficient of local head loss; Q is the flow rate; D is the pipe diameter; $K_x = \partial A / \partial x$ is the geometric divergence rate of the draft tube cross section along the x direction; L_p is the total length of the cone tube; a is the velocity of water striking wave; ρ is the density of water; μ'' is the expansion viscosity.

267

268

269

270

271

272

273

The cavitation spiral vortices are equivalent to an external forcing function of the system and the integration of an additional voltage source in each electrical grid under the partial load. The voltage source is a momentum source corresponding to the force generated by the vortex [35]. Because the equivalent circuit of each section of the tube cone is similar, only one section of the water head and the flow calculation formula is listed. Based on Kirchhoff's voltage law and Eq. (16), the equivalent circuit model of the one-dimension draft tube model is as bellow. Therefore, the water head and flow rate of the draft tube are calculated by Eq. (17).

$$\begin{cases} \frac{dQ_1}{dt} = \frac{2}{L} \left\{ h_1 - h_{1+1/2} - \left[\frac{1}{2}(R_\lambda - R_d - J_1) + R_\mu \right] Q_1 - \left(\frac{J_1}{2} - R_\mu \right) Q_2 \right\} \\ \frac{dQ_2}{dt} = \frac{2}{L} \left\{ h_{1+1/2} - h_2 - \left(\frac{J_2}{2} - R_\mu \right) Q_1 - \left[\frac{1}{2}(R_\lambda - R_d - J_2) + R_\mu \right] Q_2 \right\} \\ \frac{dh_{1+1/2}}{dt} = \frac{Q_1 - Q_2}{C_c} \end{cases} \quad (17)$$

275 Where Q_1 and Q_2 are the upper and lower flow rate in the first section of the draft tube; h_1 , h_2 , and $h_{1+1/2}$
276 are the upper, middle, and lower water head in the first section, respectively; J_1 and J_2 are the upper and
277 lower convection term in the first section.

278 The method proposed in this study improves the model of the one-dimensional hydro-turbine
279 governor system. The one-dimensional model does not simulate the signal of the high frequency part of
280 the draft tube pressure fluctuation, and the simulation accuracy of the vortex rope excitation information
281 is relatively low compared with the three-dimensional model. However, the three-dimensional model
282 requires a lot of parameters and is difficult to connect with the hydro-turbine governor system. The
283 purpose of this study is to consider the effect of the draft tube vortex rope on the hydro-turbine governor
284 system. Therefore, this study proposes a one-dimensional hydro-turbine governor system model
285 considering vortex rope excitation.

286 2.3 The calculation flow during a transition process for HGS

287 A transition process is the process that HGS goes through when moves from one steady state to
288 another. Because the transition process calculation involves the knowledge of the initial steady state of
289 HGS, this study divides the transition process calculation into two parts: the steady state calculation and
290 the transition process calculation.

291

292 2.3.1 The steady state condition

293 Calculating the initial steady state of the system is indispensable to accurately calculate the transition
294 process for HGS. The upstream and downstream water level, the boundary conditions of the pipe, the unit
295 speed n_0 and the hydro-turbine head initial value h_t are given, and the guide vane opening y is set as a
296 constant value. Based on the initial parameters, an iteration steps procedure is adopted as follows [36]:

297 **Step 1:** From the turbine head h_t , the unit speed n_0 and the runner diameter D_t , the unit flow Q_{11} and
298 the turbine flow Q_t are obtained by $n_{11}=n_0D_t/\sqrt{h_t}$, the hydro-turbine characteristic curve ($Q_{11}=f(n_{11}, y)$)
299 and $Q_t=Q_{11}D_t^2\sqrt{h_t}$;

300 **Step 2:** The water head H_{pl} and H_{pO} at the inlet and outlet of the hydro-turbine are obtained by using
301 MOC and the one-dimension draft tube model to solve the pipe parameters. The hydro-turbine head H_t is
302 calculated as: $H_t=H_{pl}-H_{pO}$;

303 **Step 3:** If $|(h_t-H_t)/H_t| \leq \varepsilon$, the hydro-turbine head H_t meets the required accuracy (ε) and the iterative
304 procedure is terminated; otherwise set $h_t=(h_t+H_t)/2$ and return to **Step 2**.

305 The flow chart of the initial condition calculation is shown in Fig. 5(a).

306

307 2.3.2 The transition process

308 From a steady state condition, the HGS is enter into a transition process if some parameters are
 309 modified (i.e. the guide vane opening y). The guide vane opening y is modeled as a time-dependent
 310 function to simulate the guide vane movement. The transition process is identified using the following
 311 iterative procedure [36]:

312 **Step 1:** Set the initial values of the hydro-turbine water head H_p and speed n_p ;

313 **Step 2:** Calculate the unit speed $n_{11}=n_p D_1/\sqrt{H_p}$;

314 **Step 3:** Compute the unit flow rate Q_{11} and the hydro-turbine flow rate Q_t from $Q_{11}=f(n_{11}, y)$ and
 315 $Q_t=Q_{11}D_i^2\sqrt{h_i}$;

316 **Step 4:** H_{pI} and H_{pO} at the inlet and outlet of the hydro-turbine are obtained according to MOC and
 317 the draft tube model; the updated hydro-turbine water head H_t is obtained according to $H_t=H_{pI}-H_{pO}$;

318 **Step 5:** If $|(H_p-H_t)/H_t|\leq\xi_1$, the desired accuracy for the water head is reached; otherwise set
 319 $H_p=H_p+\alpha(H_t-H_p)$ and return to **Step 1**;

320 **Step 6:** Compute the unit torque M_{11} from $M_{11}=f(n_{11}, y)$, and the torque M_t from $M_t=M_{11}D_i^3H_t$;

321 **Step 7:** If $|(n_p-n_t)/n_t|\leq\xi_2$, the hydro-turbine speed n_t has been calculated with the desired accuracy;
 322 otherwise set $n_p=n_p+\beta(n_t-n_p)$ and return to **Step 1**. If meet, solve the model of the water diversion system
 323 and draft tube;

324 **Step 8:** Increment the time as $t=t+\Delta t$ and repeat the above steps until the end of the transition process.

325 The flow chart of the transition process calculation is shown in Fig. 5(b).

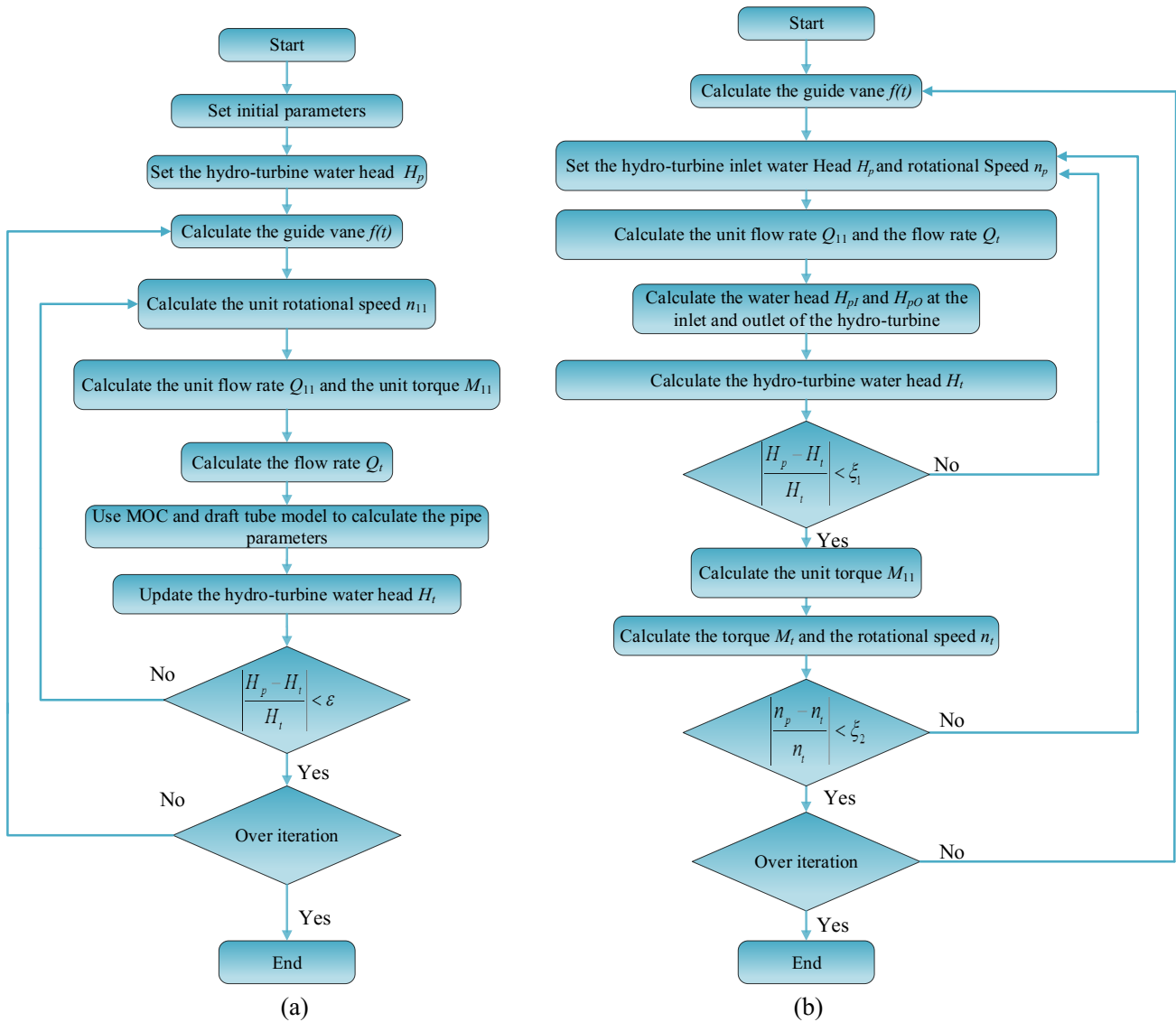


Fig. 5 The flow chart of the steady state calculation (a) and the transition process calculation (b).

326
327

328
329

3. The model validation

331 The model is validated using the experiment data provided by Norwegian University of Science and
 332 Technology under the Francis-99 workshop series [37]. In view of the actual layout of the hydraulic
 333 laboratory, a nonlinear model of HGS with one tunnel for one unit including the cone tube of the draft
 334 tube (Model I) is established by the method proposed in this study. Similarly, the model without the cone
 335 tube of the draft tube (Model II) is established regarding the draft tube cone as a straight tube. Both Model
 336 I and Model II are used to simulate the load reduction. The simulation results of Model I and Model II
 337 are compared against the results of the laboratory experiment to verify the correctness of the model
 338 established in this study. Finally, the optimum ΔT is found by analyzing the relationship between the
 339 different ΔT and the characteristics of the draft tube pressure fluctuation.

340

3.1 The experimental parameters and characteristic curve processing

341

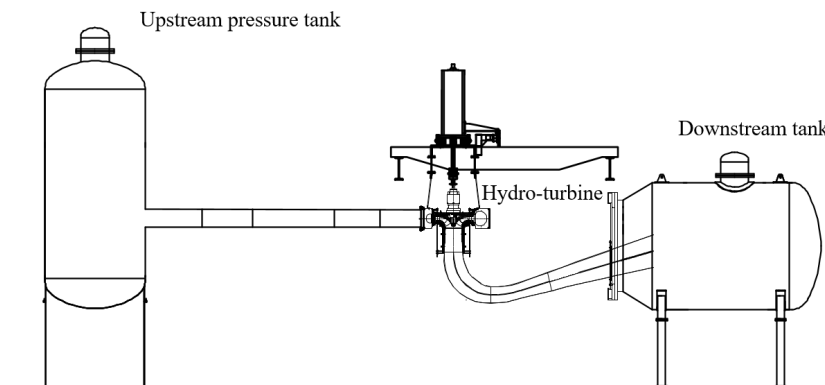
342 The test rig used (Fig. 6) for this model validation work is located at the Water Power Laboratory,
 343 Norwegian University of Science and Technology, Trondheim, Norway. The hydro-turbine, operating
 344 with an open loop circuit, is scaled down from prototype 1:5.1 [38]. Besides the runner with a total of 15
 345 splitters and 15 full length blades, the model includes 14 stay vanes inside the volute casing, 28 guide
 346 vanes and an elbow draft tube. Fig.7 [37] shows the sensor locations in the cone tube of the draft tube and
 347 the comprehensive characteristic curve is shown in Fig. 8 [37].

348 The experimental data of the load reduction are used to verify the established numerical model. Both
 349 the experiment and the simulation use a constant speed which of 332.59 rpm. The guide vane opening
 350 adopts a one-step closing strategy. Besides, the initial parameters under the best efficiency point (BEP)
 351 condition are shown in Table 1 [37]. Based on these conditions, the load change is initiated going from
 352 BEP to part load (PL).

353 **Table 1** The initial parameters under best efficiency point conditions [37].

parameter	unit	BEP	uncertainly
Guide vane angle	°	9.84	±0.04°
net head	m	11.94	±0.011%
discharge	m ³ s ⁻¹	0.2	±0.1%
Torque to generator	N m	616.13	±0.03%
friction torque	N m	4.52	±1.5%
Runner rotation speed	rpm	332.59	±0.05%
Casing inlet pressure-abs	kPa	215.57	±0.047%
Draft tube outlet pressure-abs	kPa	111.13	±0.001%
Hydraulic efficiency	%	92.39	± 0.14%
Water density	kg m ⁻³	999.8	± 0.01%
Kinematic viscosity	m ² s ⁻¹	9.57E-07	--
Gravity	m s ⁻²	9.82	--
sampling time	s	10	--

354



355

356

357

358

Fig. 6 The schematic diagram of the experimental equipment [37].

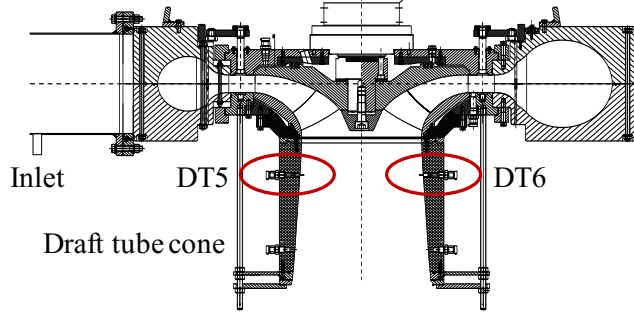


Fig. 7 The sensor locations in the draft tube cone [37].

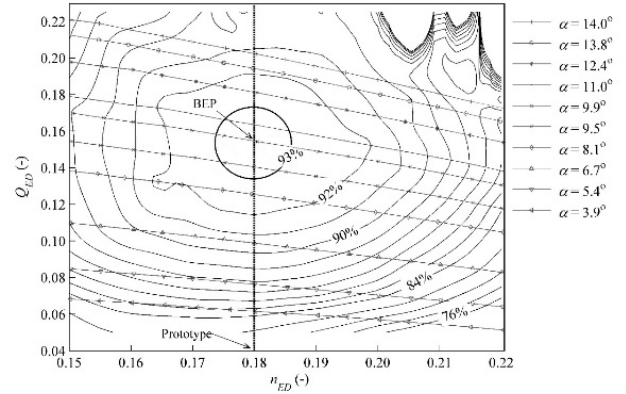


Fig. 8 The comprehensive characteristic curve of the hydro-turbine model [37].

Based on TPS interpolation, the comprehensive characteristic curve in Fig.8 is transformed and the results are shown in Fig. 9. Variables n_{11} , M_{11} , Q_{11} and y in Fig. 9 represent the unit speed, torque, flow rate of the hydro-turbine and guide vane, respectively.

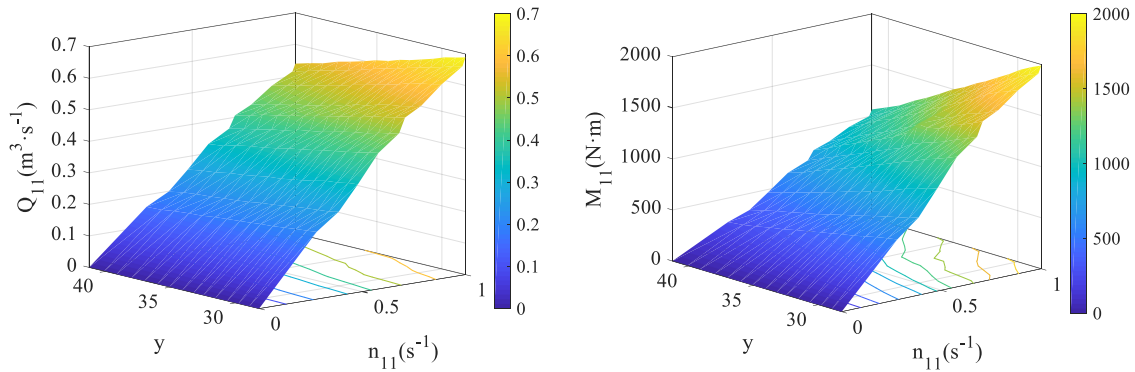


Fig. 9 The characteristics of the hydro-turbine flow and torque.

From Fig. 9, the unit flow and torque corresponding to the different guide vane and different unit speed are expanded in the three-dimensional space to provide a reasonable data base for the subsequent transition process.

3.2 Model I vs experiment data

The adopted parameters of Model I are shown in Table 2. A one-stage closing law is adopted and the guide vane closing time and the total simulation time are 2.43s and 10s, respectively. The simulation step used is 0.002s.

376

Table 2 The parameters of Model I.

Model parameter	Physical meaning	Unit	Numerical value
TL	Length of the tunnel	m	13
STL	Length of the surge tank	m	2.3
$STBL$	Length of the penstock behind the surge tank	m	18
CTL	Length of the cone tube	m	0.341
DTL	Length of the draft tube	m	10
$DTSTL$	Length of the surge tank behind the draft tube	m	3.2
$DTSTBL$	Length of the tail tunnel behind the surge tank	m	15
TD	Diameter of the tunnel	m	0.36
$STBD$	Diameter of the penstock behind the surge tank	m	0.35
CTD_{out}	Diameter of the cone tube outlet	m	0.42
CTD_{in}	Diameter of the cone tube inlet	m	0.349
DTD	Diameter of the draft tube	m	0.45
$DTSTBD$	Diameter of the tail tunnel behind the surge tank	m	0.3

377

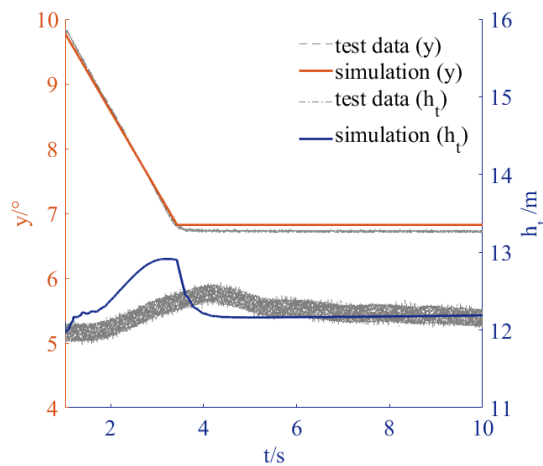
378

379

380

381

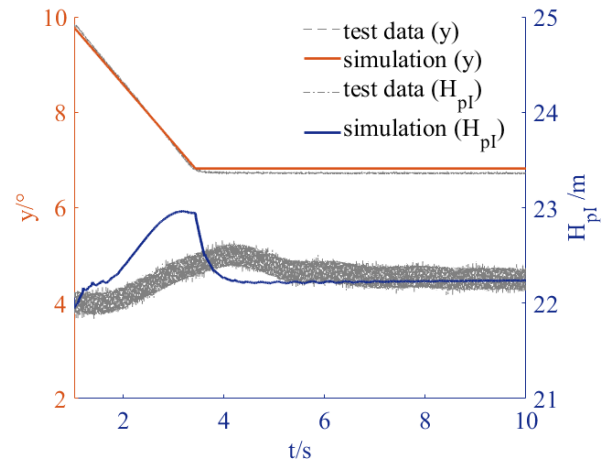
The load reduction simulation of Model I is carried out based on the above premise, and the water head, the inlet water head and the flow results are compared with the experimental results. The results are shown in Fig. 10 and Table 3.



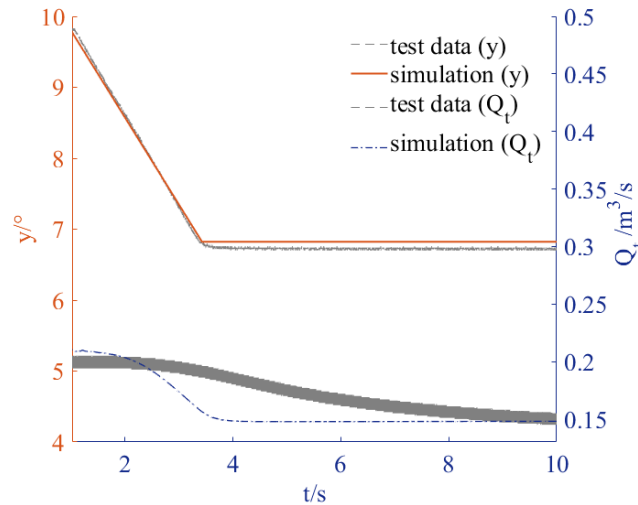
382

383

(a) The hydro-turbine water head comparison diagram.



(b) The hydro-turbine inlet water head comparison diagram.



(c) The hydro-turbine flow comparison diagram.

Fig. 10 The comparison diagram of Model I simulation results and experimental results.**Table 3** The comparison of Model I simulation results and experimental results for the water head, the inlet water head and the flow rate.

Variable	Model	The initial value	The maximum value	The final value
Water head	The simulation	11.97m	12.91m	12.19m
	The experiment	11.94m	12.50m	12.16m
	The error	0.25%	3.28%	0.25%
Inlet water head	The simulation	22.06m	22.96m	22.24m
	The experiment	22.01m	22.53m	22.27m
	The error	0.23%	1.9%	0.13%
Flow	The simulation	0.21m ³ /s	/	0.148m ³ /s
	The experiment	0.20 m ³ /s	/	0.15 m ³ /s
	The error	5%	/	1.35%

Fig. 10 (a) shows the comparison of the results obtained from Model I and the experimental results of the hydro-turbine water head during the load reduction. The Model I is able to reproduce the water head consistently with the experimental data, although it is possible to notice that the start time of the water head change in the simulation occurs earlier than the experimental results, which is caused by three reasons: the assumption errors, the internal flow field characteristics and as well the possible experimental errors. First, the simulation assumes that the fluid is a continuous medium, and each physical quantity changes continuously. Therefore, when the guide vane changes suddenly, the water head also changes simultaneously in the simulation. Second, the flow field characteristics in the hydro-turbine changes because of the eddy current when the guide vane opening changes, which hinder the change of the water head in the experiment. Finally, there is a delay when the experimental equipment records the data. The above reasons cause the start time of the water head change in the simulation is earlier than the experimental results. From Fig.10 (a) and Table 3, comparing the experimental data, the initial simulated

403 water head is 11.97m after 1s stable condition calculation, which is basically consistent with the
 404 experimental data (i.e., 11.94m). The simulation error is 0.25%. From 1s to 3.43s, the system enters the
 405 transition process. As the guide vanes are closed, the simulated water head gradually increases to 12.91m,
 406 which is higher than the maximum experimental water head (i.e., 12.5m). The simulation error is 3.28%.
 407 From 3.43s to 6s, the guide vane stops action and the opening remains unchanged. The simulated water
 408 head decreases from 12.91m to 12.16m, and the experimental water head decreases from 12.5m to 12.21
 409 m. After 6s, the system basically enters a stable operation state. At the end of 10s, the simulated water
 410 head stabilizes to 12.19m, which is basically consistent with the experimental inlet water head (i.e.,
 411 12.16m). The simulation error is 0.25%. In general, the simulation value error of the water head is within
 412 $\pm 3.3\%$, so the Model I is reliable for simulating the water head of the hydro-turbine in the transition
 413 process.

414 Fig. 10 (b) shows the results for the hydro-turbine inlet water head during the load reduction. The
 415 inlet water head of Model I is again in general agreement with the experimental data, but again the start
 416 time of the inlet water head change in the simulation is also earlier than the experimental results. The
 417 reasons are the same as the three reasons causing the water head error. From Fig. 10 (b) and Table 3,
 418 comparing the experimental data, the initial simulated inlet water head is 22.06m after 1s stable operation,
 419 which is slightly higher than the experimental result (i.e., 22.01m) and the error is 0.23%. From 1s to
 420 3.43s, the system enters the transition process. As the guide vanes are closed, the simulated inlet water
 421 head gradually increases to 22.96m, which is higher than the experimental maximum value of 22.53m.
 422 The simulation error is 1.9%. From 3.43s to 6s, the guide vane stops action and the opening remains
 423 unchanged. The simulated inlet water head decreases to 22.23m. Correspondingly, the experimental inlet
 424 water head decreases to 22.32m. After 6s, the system basically enters a stable operation state. At the end
 425 of 10s, the simulation inlet water head stabilizes to 22.24m, which is basically consistent with the
 426 experimental inlet water head (i.e., 22.27m). The simulation error is 0.13%. In general, the simulation
 427 value error of the inlet water head is within $\pm 2\%$, so the Model I is reliable for simulating the inlet water
 428 head of the hydro-turbine in the transition process.

429 Fig. 10 (c) shows the comparison of the Model I simulation results and the experimental results of
 430 the hydro-turbine flow rate during the load reduction. From Fig.10 (c), the flow rate of Model I is basically
 431 consistent with the experimental data, but the start time of the flow rate change in the simulation is also
 432 earlier than the experimental results. The reasons are the same as the three reasons causing the water head
 433 error. From Fig. 10 (c) and Table 3, comparing the experimental data, the initial simulated flow rate is
 434 $0.21\text{m}^3/\text{s}$ after 1s stable operation, which is slightly higher than the experimental result (i.e., $0.2\text{m}^3/\text{s}$) and
 435 the error is 5%. From 1s to 3.43s, the system enters the transition process. As the guide vanes are closed,
 436 the simulated flow rate decreases to $0.16\text{m}^3/\text{s}$. From 3.43s to 4s, the guide vane stops action and the
 437 opening remains unchanged. The simulated flow rate is reduced from $0.16\text{m}^3/\text{s}$ to $0.148\text{m}^3/\text{s}$. In the
 438 process of the flow rate reduction, the rate of the simulated flow rate change is higher than that of the
 439 experimental flow rate change. The reason is that there is a certain error between the characteristic curve
 440 processed by TPS interpolation and the real dynamic characteristics of the hydro-turbine. Besides, the
 441 control of the flow rate in the experiment also affects the rate of the flow rate change. At the end of 10s,
 442 the simulation flow rate stabilizes to $0.148\text{m}^3/\text{s}$, which is basically consistent with the experimental flow
 443 rate (i.e., $0.15\text{m}^3/\text{s}$). The simulation error is 1.35%. In general, the simulation value error of the flow rate

444 is within $\pm 5\%$, so the Model I is reliable for simulating the flow rate of the hydro-turbine in the transition
 445 process.

446 In general, the simulation value error of the flow rate is within $\pm 5\%$. Model I can be considered a
 447 reliable model for simulating the flow rate of the hydro-turbine in the transition process. From the above
 448 analysis, the simulation value errors of the water head, the inlet water head and the flow rate for Model I
 449 are within $\pm 3.3\%$, $\pm 2\%$ and $\pm 5\%$, respectively showing the correctness of Model I.

450

451 3.3 Model I vs Model II & experiment data

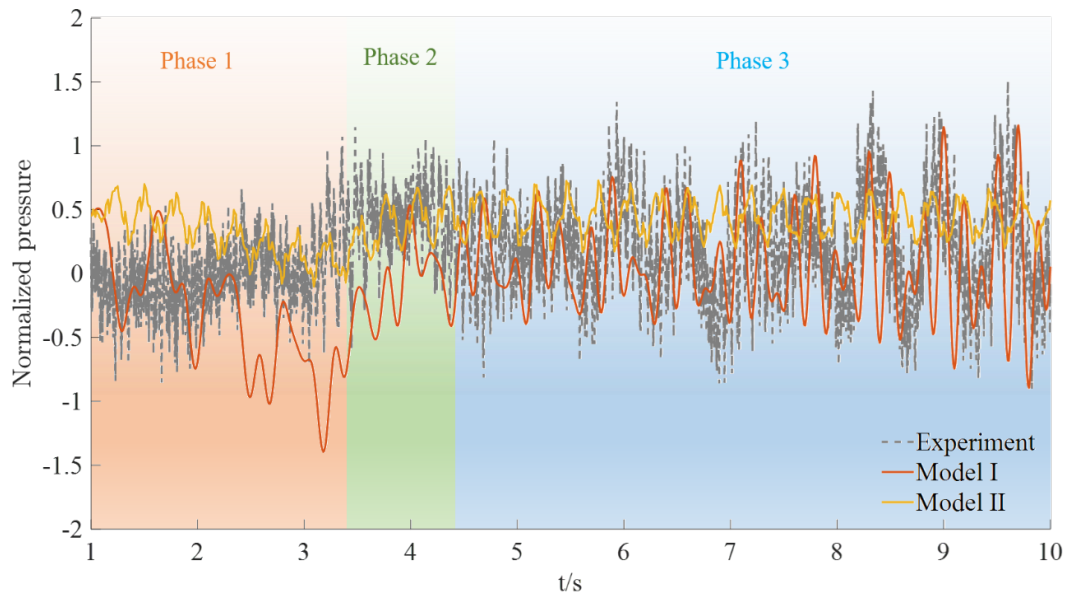
452 The results of Model I and Model II are analyzed in the time and frequency domain to verify that
 453 Model I is more practical than Model II.

454

455 3.3.1 The time domain validation

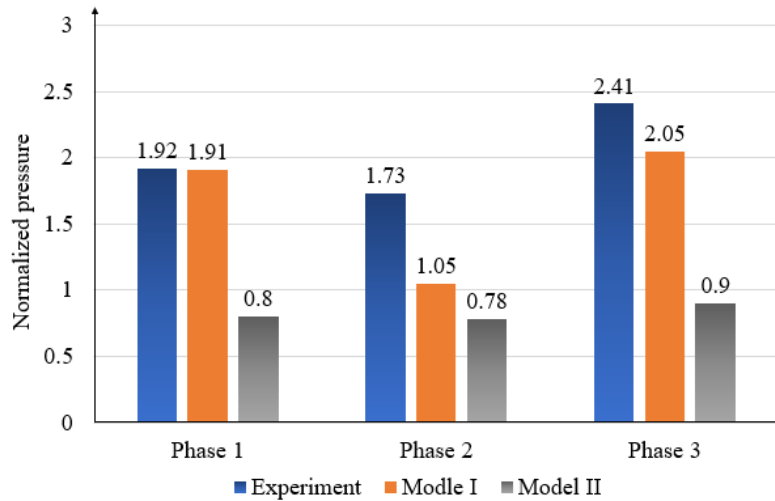
456 The results of Model I and Model II are normalized based on the rated pressure to compare the
 457 pressure fluctuation at the draft tube inlet. The results are divided into Phase 1, Phase 2 and Phase 3,
 458 according to the state of the guide vane. The time-domain diagram of the normalized pressure for the
 459 simulation (Model I & Model II) and the experiment is show in Fig. 11. Fig. 12 shows the amplitude of
 460 the normalized pressure.

461



462

463 **Fig.11** The time-domain diagram of the normalized pressure at the draft tube for Model I, Model II and the experiment.



464

Fig. 12 The amplitude of the normalized pressure at the draft tube for Model I, Model II and the experiment.

465

466

467

468

469

470

471

472

473

474

475

476

477

478

479

480

481

482

483

484

485

486

487

488

489

490

491

492

493

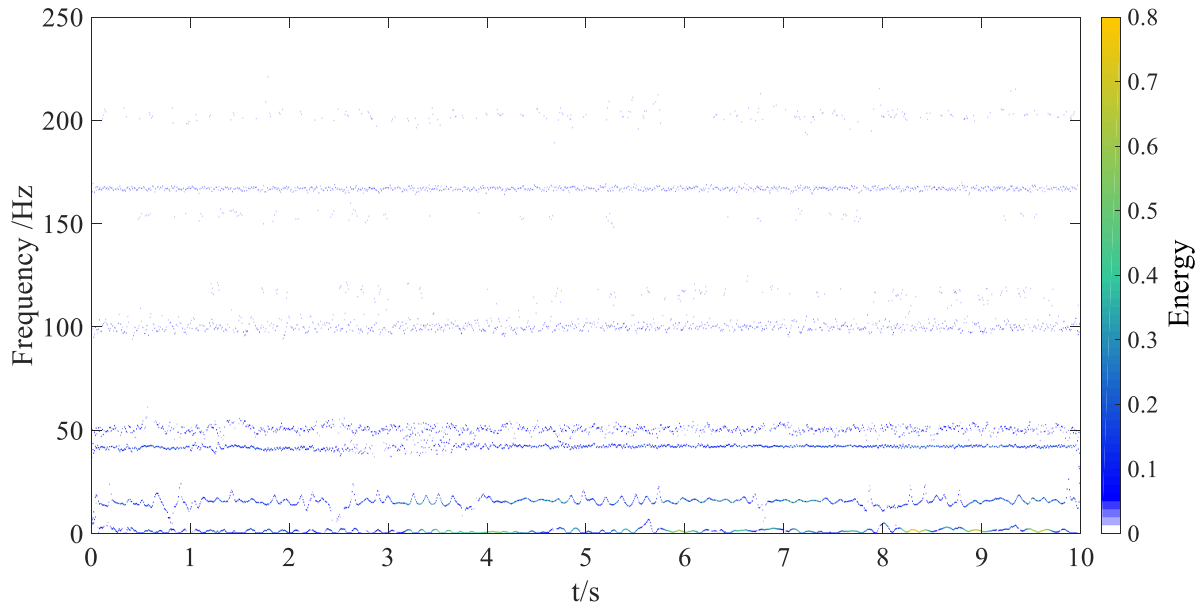
From Fig. 11 it can be seen that the normalized pressure of Model I and Model II are both higher than the experimental data after 1s stable operation. The reason is that the simulations use the constant reservoir boundary conditions, while this cannot be guaranteed during the experiments. In addition, the setting of the friction coefficient of the simulation model is different from that of the laboratory experiment, which leads to the difference between the initial value of the simulation and the experiment. From 1s to 3.43s (i.e., Phase 1), the guide vane is closed and the simulated normalized pressure of Model I and Model II are both decreased, which are consistent with the experimental data. But the reduction of Model I is larger than the experimental results. This is mainly because the local backflow occurs at the measuring point during the experiment, resulting in the local pressure rise. The simulation does not simulate this phenomenon. From 3.43s to 4.3s (i.e., Phase 2), the guide vane stops action and the inlet pressure of the draft tube rises rapidly to dynamic equilibrium. The simulated inlet pressure of Model I rises faster compared with the experiment. This is mainly because the simulation does not simulate the effect of the internal flow field characteristics. After 4.3s (i.e., Phase 3), the pressure fluctuation tends to be dynamically balanced, and the internal flow field is also dynamically stable. From Fig. 11, the simulation result of Model II is quite different from the experiment, while the simulation result of Model I is basically consistent with the experiment in terms of the value and the trend.

From Fig. 12, in Phase 1, the amplitudes of the normalized pressure for experiment and Model I are basically equal, which are 1.92 and 1.91, but Model II result is 0.8. In Phase 2, the amplitudes of the normalized pressure for experiment, Model I and Model II are 1.73, 1.05 and 0.78, respectively. In Phase 3, the amplitudes of the normalized pressure for experiment and Model I are basically equal, which are 2.41 and 2.05, but Model II result is 0.9. Therefore, Model 1 is closer to the experiment than Model 2 from the perspective of the amplitude of the normalized pressure.

In summary, the simulation result of Model I reflects the pressure changes at the draft tube inlet in terms of the value and the trend during the transition process, compared the experimental results. However, Model II can only calculate the mean pressure at the draft tube inlet, which does not reflect the actual situation. Therefore, the calculation results of Model I are closer to the experimental results than those of Model II at the draft tube inlet in the time domain.

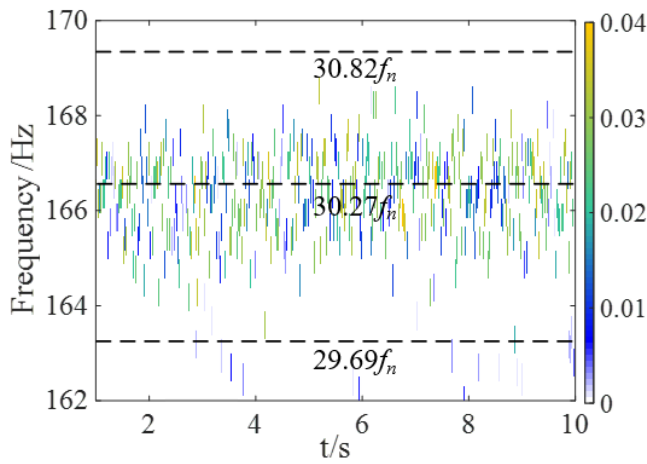
494 **3.3.2 The frequency domain validation**

495 The simulation data and the experimental data are compared in the frequency domain by using the
 496 variational mode decomposition (VMD) to further study the vortex rope excitation characteristics and
 497 verify the applicability of Model I. The corresponding time-frequency spectrogram are obtained in Figs.
 498 13, 14 and 15.
 499



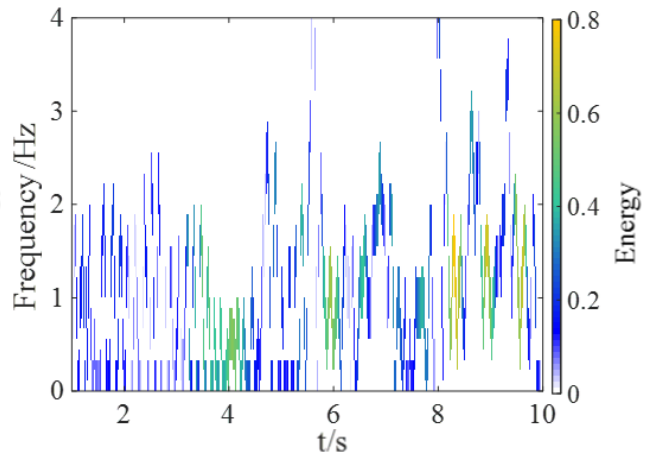
500
 501

(a)



502
 503

(b)



(c)

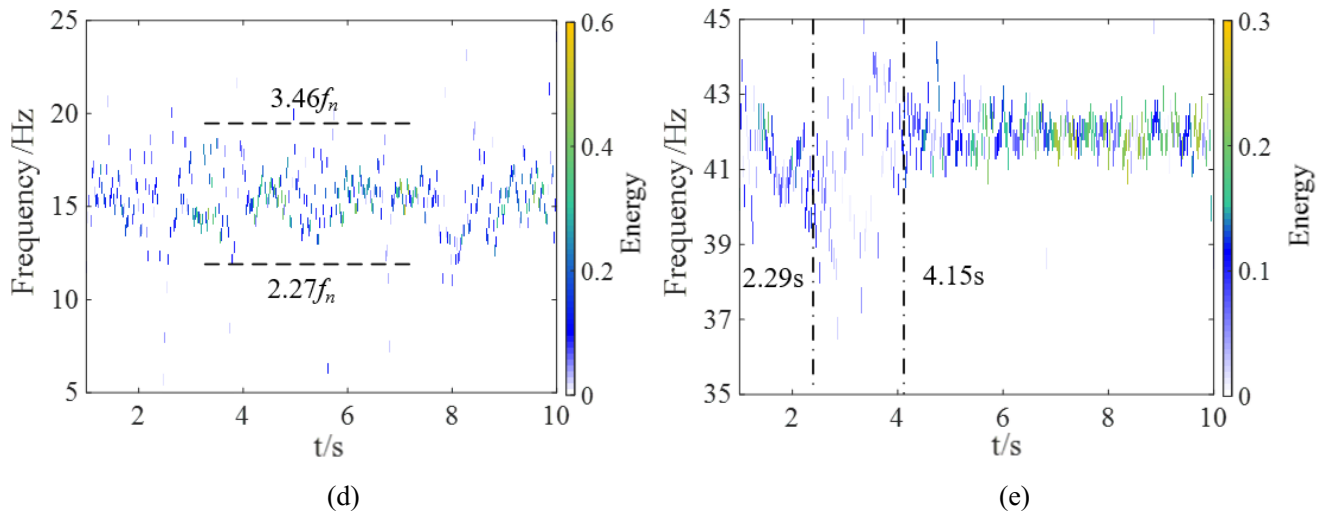


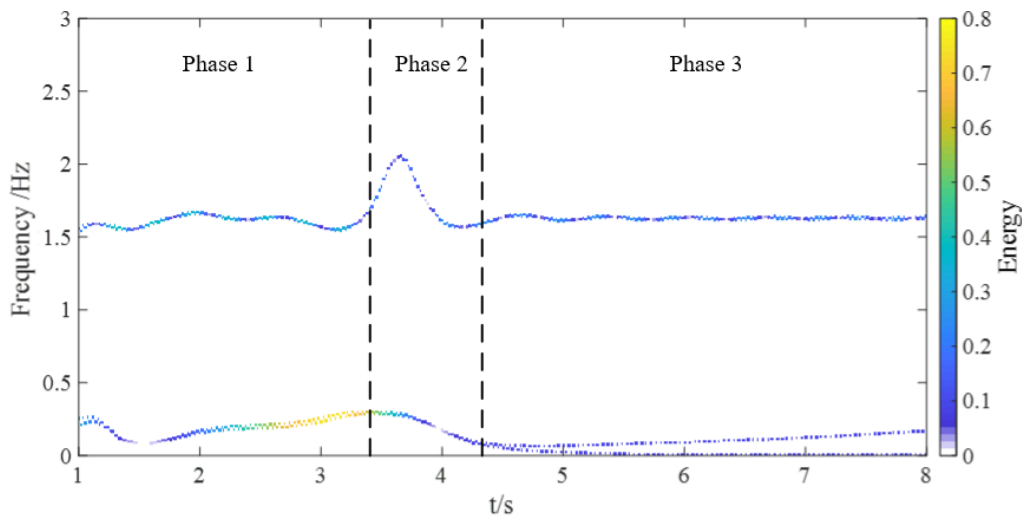
Fig. 13 The time-frequency spectrum of the vortex rope excitation for the experiment in the different frequency bands.

Fig. 13 shows the time-frequency spectrum of the vortex rope excitation for the experiment. Fig. 13 (a) is the time-frequency spectrum including all frequency components. Fig. 13 (b), (c), (d), and (e) are the time-frequency spectra of the high frequency signal, the low frequency signal, the upstream and downstream standing waves, respectively. Fig. 13 (a) shows all characteristic information of the vortex rope excitation in the whole frequency band. This subsection selects some typical frequency bands for the specific description to further study the vortex rope excitation characteristics. Fig. 13 (b) is the time-frequency spectrum of the high frequency signal with a center frequency of $30.27f_n$ (f_n is the rotational frequency, 5.5Hz) [39-40], and the frequency fluctuation range is $29.69f_n$ to $30.82f_n$. With the closing of the guide vane, the internal flow field of the hydro-turbine changes, causing the blade resonance. In this frequency band, the energy fluctuation range is 0~0.04. Fig. 13 (c) is the time-frequency spectrum of the low frequency signal. Within 1s~1.69s, the guide vane is closed. The vortex rope is very small, and the effect of the vortex rope excitation is not obvious due to the influence of the flow inertia. The frequency band is wide under the vortex rope excitation, but the energy fluctuation range in the frequency band is small, which is 0~0.18. Within 1.69s~3.43s, the guide vane continues to close, and the vortex rope develops rapidly. The frequency fluctuation changes irregularly under the vortex rope excitation, and the energy fluctuation range is 0~0.28. Within 3.43s~4.3s, the vortex rope continues to develop, the frequency fluctuation under the vortex rope excitation decreases, and the energy fluctuation range is 0~0.6. Specifically, the high-energy frequency band is mainly concentrated in 0~1.09Hz. Within 4.3s~10s, the vortex rope develops to a stable state when the guide vane stops closing, and the vortex rope excitation presents the regular periodic frequency fluctuations. The energy fluctuation range is 0~0.8, and the high-energy frequency band is mainly concentrated in 0.23~2.4Hz. Fig. 13 (d) is the time-frequency spectrum of the upstream standing wave with a center frequency of 15.8Hz ($2.87f_n$). The energy fluctuation occurs from 3.18s to 7.41s with the range of 0~0.58, and the frequency fluctuation range is $2.27f_n$ to $3.46f_n$. The energy fluctuation period is different from the guide vane closing period (1~3.43s). The reason is that the fluctuation of the hydraulic excitation increases due to the closing of the guide vane. And it takes time for the energy to be transferred along the pipe to the draft tube inlet. Fig. 13 (e) is the time-frequency spectrum of the downstream standing wave with a center frequency of 41.8Hz ($7.6f_n$). The frequency fluctuation

535 with the low energy (0~0.14) and the wide frequency band appears in the downstream standing wave from
 536 2.29s~4.15s. The frequency fluctuation period is different from the guide vane closing period. The reason
 537 is the same as the reason causing the difference between the energy fluctuation period and the guide vane
 538 closing period in Fig. 13 (d).

539 The above frequencies include the high frequency components, which do not be simulated by the
 540 one-dimensional simulation model. Model I mainly focuses on the vortex rope in the draft tube, and the
 541 frequency of the vortex rope is mainly concentrated in $(1/6\sim 1/2) f_n$ [39-40], which is the low frequency
 542 components. Therefore, the time-frequency analyses are conducted on the simulation results of Model I
 543 and Model II in the low frequency to verify the superiority and reliability of Model I.

544



545

546 **Fig. 14** The time-frequency spectrum of the normalized pressure at the draft tube for Model I in the low frequency.

547

548 Fig. 14 shows the time-frequency spectrum of the normalized pressure at the draft tube for Model I.
 549 The three phases in Fig. 14 are analyzed respectively.

550 In Phase 1 (1s~3.43s), the hydro-turbine governor system is in the transitional process, because of
 551 the closing of the guide vane. The hydraulic excitation changes sharply and the vortex rope appears.
 552 Specifically, from 1s~1.4s, the vortex rope is very small. The time-frequency domain information of each
 553 frequency band changes little, and the energy fluctuation range is 0~0.39. Therefore, the vortex rope
 554 excitation is in the stage of the slow change. From 1.4s~3.43s, the wake vortex zone is developing rapidly.
 555 The time-frequency domain information of the lower frequency band becomes change, and the energy
 556 fluctuation range is 0~0.77. Therefore, the vortex rope excitation is in the stage of the rapid change.

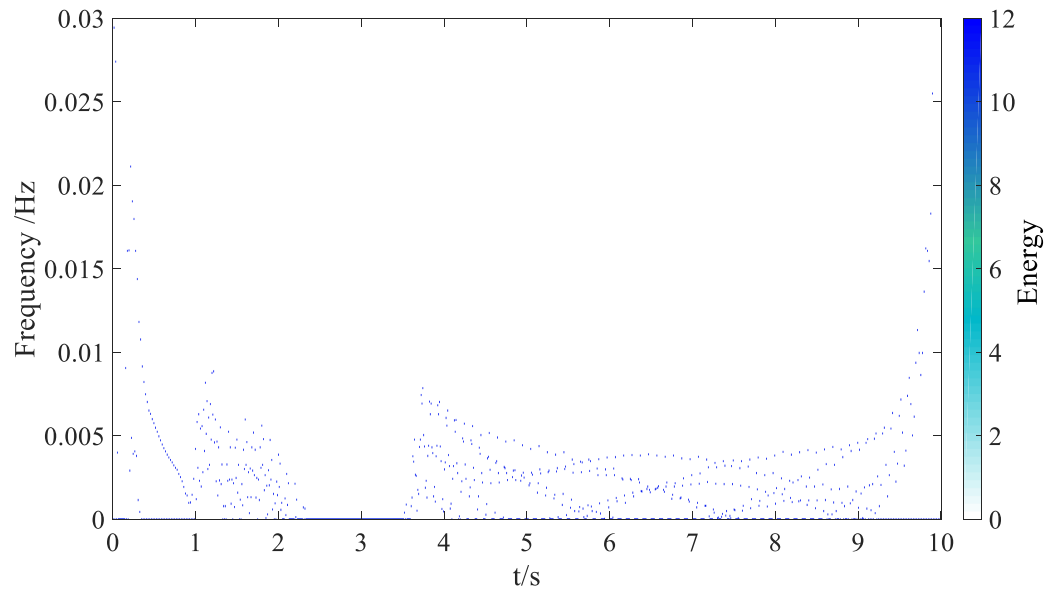
557

558 In Phase 2 (3.43s~4.3s), the vortex rope excitation energy of each frequency band decreases, because
 559 the guide vane stops closing. From Fig. 14, the upper frequency band affected by the precession frequency
 560 of the vortex rope shows the large frequency fluctuation, which increases rapidly from 1.6Hz to 2.06Hz
 561 and then returns to 1.56Hz. And the energy fluctuation range is 0~0.23. The frequency of the lower
 562 frequency band decreases slowly from 0.29Hz to 0.067Hz, and the energy decreases rapidly from 0.57
 563 to 0.08. The reason is that the vortex rope excitation is transitioning from the unstable state to the stable
 state.

564 In Phase 3 (4.3s~10s), all hydraulic excitations are in equilibrium, and the vortex rope also maintains
 565 a stable development shape. The time-frequency domain information of each frequency band shows the
 566 stable frequency fluctuation. The frequency fluctuations of the upper and lower frequency band are
 567 1.6Hz~1.66Hz and 0.01Hz~0.16Hz, respectively. This shows that the vortex rope excitation at the draft
 568 tube inlet is in a stable periodic fluctuation stage.

569 From the above analysis, Model I basically reflects the vortex rope excitation in the frequency
 570 domain.

571



572

573 **Fig. 15** The time-frequency spectrum of the normalized pressure at the draft tube for Model II in the low frequency.

574

575 From Fig. 15, the frequency of the high-energy section for Model II is 0Hz, indicating that the vortex
 576 rope excitation is a constant value (i.e., 11.2) of energy. And there are no characteristic frequency bands
 577 such as the vortex rope precession frequency and its harmonics in the whole frequency band. These
 578 characteristics are different from the actual situation of the vortex rope excitation in the transition process.
 579 Therefore, Model II do not reflect the characteristic information of the vortex rope excitation in the
 580 frequency domain.

581 The comparisons of the maximum frequency and maximum energy fluctuation for different methods
 582 in the load reduction are shown in Table 4 to further quantify and compare the performance of different
 583 methods in the frequency domain.

584

585 **Table 4** The comparison of the maximum frequency and maximum energy fluctuation for different methods in the
 586 load reduction. The maximum frequency is defined as F_{max} , and the maximum energy fluctuation is defined as EF_{max} .

	Experiment	Model I	Model II
EF_{max}	0.8	0.77	11.2
F_{max} (Hz)	2.4	2.06	0

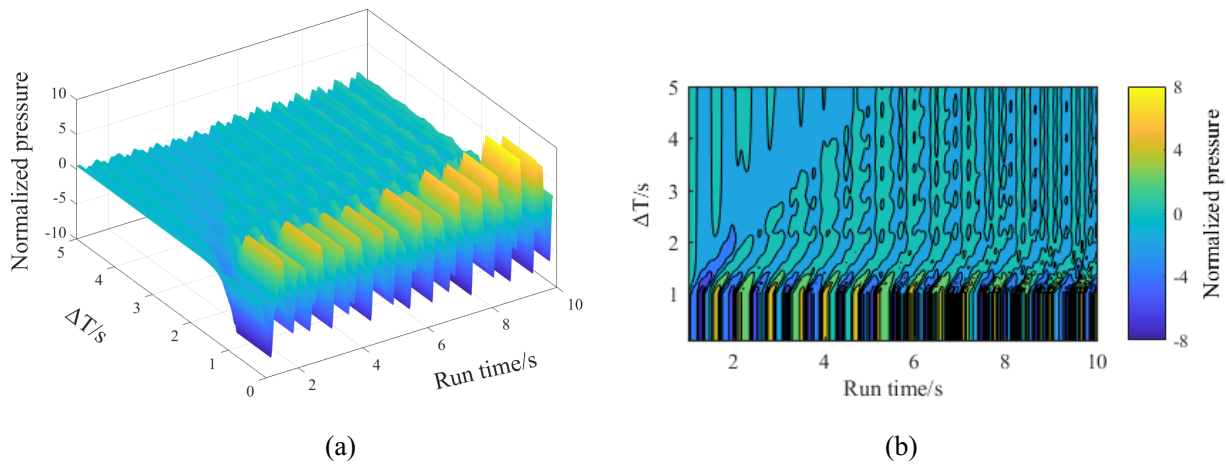
587 As shown in Table 4, the results of experiment, Model I and II show that EF_{max} in the low frequency
 588 are 0.8, 0.77 and 0, respectively, and F_{max} in the low frequency are 2.4Hz, 2.06Hz and 11.2Hz,
 589 respectively. The results of Model I are close to those of experiment in the frequency domain, which
 590 reflect the vortex rope excitation, while Model II do not reflect this excitation. Therefore, Model I is more
 591 practical in the frequency domain.

592 In summary, Model I is more suitable for the actual situation than Model II in both time and frequency
 593 domain.

594 3.4 The effect of the guide vane closing time on the draft tube pressure fluctuation

595 This subsection studies the relationship between the guide vane closing time (ΔT) and the draft tube
 596 pressure fluctuation during the load reduction to reduce the influence of the pressure fluctuation on the
 597 unit. The guide vane closing law follows the previous linear closing law. The evolution process and
 598 contour map between ΔT and the normalized pressure fluctuation at the draft tube inlet are shown in Fig.
 599 16.

600



601

602

603 **Fig. 16** The evolution process (a) and contour map (b) between different the guide vane closing time ΔT and the
 604 normalized pressure fluctuation at the draft tube inlet.

605 From Fig. 16 (a) and (b), when $\Delta T \leq 1.60s$, the pressure fluctuation at the draft tube inlet is severe
 606 and the amplitude is large, because of the fast guide vane closing speed. When $\Delta T \geq 1.60s$, the pressure
 607 fluctuation is in the development stage during the guide vane closing time, and forms a stable fluctuation
 608 form after the guide vane stops. Furthermore, the longer ΔT is, the more stable the development stage of
 609 the pressure fluctuation is, and the smaller the value of the vacuum at the draft tube inlet is. However, the
 610 vacuum degree decreases slowly with the continuous increase of ΔT . In summary, properly increasing ΔT
 611 is beneficial to reducing the pressure fluctuation at the draft tube inlet, but continuously increasing ΔT
 612 does not have much effect on reducing the pressure fluctuation. The optimum ΔT is between 1.93s and
 613 3.3s in this study.

614

615 4. Conclusions

616 Hydropower plays an important role in energy system due to its flexible regulation. With the large-
 617 scale wind power and photoelectric power connected to the power grid, hydropower units need frequent
 618 operation conversion and often operate under the off-design conditions to balance the power fluctuation.

619 The hydro-turbine governor system is affected by the draft tube vortex rope when hydropower units
620 operate under the off-design conditions. Therefore, it is very important to study the hydro-turbine
621 governor system considering the vortex rope excitation.

622 This study revises the calculation method of the water head at the draft tube inlet and applies it to
623 the hydro-turbine governor system model. The correctness and applicability of Model I is verified by
624 comparing against the experiment results in the time domain and frequency domain. Based on Model I,
625 the optimum guide vane closing time ΔT is found by analyzing the relationship between different ΔT and
626 the draft tube pressure fluctuation. The main conclusions are as follows:

627 •The inlet water head error, the water head error and the flow rate error of Model I are within \pm
628 3.3%, $\pm 2\%$ and $\pm 5\%$, respectively, compared with the experimental results in the time domain.

629 •Model I reflects the pressure change at the draft tube inlet in terms of the value and the trend during
630 the transition process, compared with the experimental results in the time domain. However, Model II can
631 only calculate the mean pressure at the draft tube inlet.

632 •The results of experiment, Model I and II show that EF_{max} in the low frequency are 0.8, 0.77 and
633 0, respectively, and F_{max} in the low frequency are 2.4Hz, 2.06Hz and 11.2Hz, respectively. The results
634 of Model I are close to those of experiment in the frequency domain, which reflect the vortex rope
635 excitation, while Model II do not reflect this excitation. The correctness and applicability of Model I are
636 verified by comparing the results of Model II and experiment.

637 Based on the above conclusions, the hydro-turbine governor system model should consider the
638 vortex rope excitation, which is close to the actual situation. Although the hydro-turbine governor system
639 model proposed in this study improved the previous model, this model still has some limitations. For
640 example, this one-dimensional model does not simulate the signal of the high frequency part of the draft
641 tube pressure fluctuation, and the simulation accuracy of the vortex rope excitation information is
642 relatively low compared with the three-dimensional model. These limitations should be considered in
643 future studies. Finally, the model proposed in this study promotes the development of the hydro-turbine
644 governor system model, and help to further study the influence of the draft tube pressure fluctuation on
645 the transient characteristics of the hydropower systems.

646

647

648 **Acknowledgements**

649 This research is supported by Chinese Universities Scientific Fund (Grant No.
650 2452020210/Z1090220172), Open Research Fund Program of State Key Laboratory of Eco-hydraulics
651 in Northwest Arid Region, Xi'an University of Technology (Grant No. K4020121034), Postdoctoral Fund
652 of Powerchina Northwest Engineering Corporation Limited (Grant No. kjb2021xz05), Scientific research
653 fund of Inner Mongolia water resources and Hydropower Survey and Design Institute (Grant No.
654 K4040121228).

655

656

References:

657 [1] Kuriqi A, Pinheiro AN, Sordo-Ward A, Garrote L. Water-energy-ecosystem nexus: Balancing competing interests at a
658 run-of-river hydropower plant coupling a hydrologic-eco-hydraulic approach. *Energ Convers Manage*

- 659 2020;223:113267.
- 660 [2] Kuriqi A, Pinheiro AN, Sordo-Ward A, Bejarano MD, Garrote L. Ecological impacts of run-of-river hydropower plants—
661 Current status and future prospects on the brink of energy transition. *Renewable and Sustainable Energy Reviews*
662 2021;142.
- 663 [3] A SK, B MJC, A BKG. Rotating vortex rope formation and mitigation in draft tube of hydro turbines – A review from
664 experimental perspective - ScienceDirect. *Renewable and Sustainable Energy Reviews* 2021;136:110354.
- 665 [4] Xiong H, Egusquiza M, Ostergaard PA, Perez-Diaz JI, Sun G, Egusquiza E, et al. Multi-objective optimization of a hydro-
666 wind-photovoltaic power complementary plant with a vibration avoidance strategy. *Appl Energ* 2021;301:117459.
- 667 [5] Yang W, Per N, Linn S, Adam W, Brennan S, Yang J, et al. Burden on hydropower units for short-term balancing of
668 renewable power systems. *Nat Commun* 2018;9:2633.
- 669 [6] Trivedi C, Agnalt E, Dahlhaug OG. Experimental study of a Francis turbine under variable-speed and discharge conditions.
670 *Renew Energ* 2018;119:447-458.
- 671 [7] Yang MH, Huang GM, Yeh RH. Performance investigation of an innovative vertical axis turbine consisting of deflectable
672 blades. *Appl Energ* 2016;179:875-887.
- 673 [8] Yang W, Norrlund P, Bladh J, Yang J, Lundin U. Hydraulic damping mechanism of low frequency oscillations in power
674 systems: Quantitative analysis using a nonlinear model of hydropower plants. *Appl Energ* 2018;212:1138-1152.
- 675 [9] Yu A, Zou Z, Zhou D, Zhen Y, Luo X. Investigation of the Correlation Mechanism between Cavitation Rope Behavior
676 and Pressure Fluctuations in a Hydraulic Turbine. *Renew Energ* 2019;147.
- 677 [10] Mulu BG, Jonsson PP, Cervantes MJ. Experimental investigation of a Kaplan draft tube – Part I: Best efficiency point.
678 *Appl Energ* 2012;93:695-706.
- 679 [11] Khan AA, Shahzad A, Hayat I, Miah MS. Recovery of flow conditions for optimum electricity generation through micro
680 hydro turbines. *Renew Energ* 2016;96:940-948.
- 681 [12] Pasche S, Gallaire F, Avellan F. Origin of the synchronous pressure fluctuations in the draft tube of Francis turbines
682 operating at part load conditions. *Journal of Fluids & Structures* 2019;86:13-33.
- 683 [13] Nishi, Michihiro, Wang, Xinming, Okamoto, Minoru, et al. Further investigation on the pressure fluctuations caused by
684 cavitation vortex rope in an elbow draft tube. *Cavitation & Gas Fluid Flow Machinery & Devices* 1994.
- 685 [14] Wu G, Dai YF, Zhan KW, Tan YC, Relations Between Flow Field and Pressure Fluctuation in Draft Tube of Francis
686 Turbine, *International Journal Hydroelectric Energy* 2000;18: 58-61. [In Chinese]
- 687 [15] A AIB, B CT. Experimental study of swirling flow from conical diffusers using the water jet control method. *Renew*
688 *Energ* 2020;152:385-398.
- 689 [16] Kirschner O, Ruprecht A, Gde E, Riedelbauch S. Experimental investigation of pressure fluctuations caused by a vortex
690 rope in a draft tube. *IOP Conference Series Earth and Environmental Science* 2012;15:2059.
- 691 [17] Favrel A, Joao GPJ, Landry C, Müller A, Nicolet C, Avellan FO. New insight in Francis turbine cavitation vortex rope:
692 role of the runner outlet flow swirl number. *J Hydraul Res* 2017;1-13.
- 693 [18] Qiang LL, Chen QJ, Research on the Pressure Fluctuation of Draft Tube Based on Field Test in Typical Heads, China
694 *Rural Water and Hydropower* 2014:137-140. [In Chinese]
- 695 [19] Khan AA, Khan AM, Zahid M, Rizwan R. Flow acceleration by converging nozzles for power generation in existing
696 canal system. *Renew Energ* 2013;60:548-552.
- 697 [20] Xu B, Chen D, Venkateshkumar M, Xiao Y, Yue Y, Xing Y, et al. Modeling a pumped storage hydropower integrated to
698 a hybrid power system with solar-wind power and its stability analysis. *Appl Energ* 2019;248:446-462.
- 699 [21] Liu QZ, Su WT, Li XB, Zhang YN. Dynamic characteristics of load rejection process in a reversible pump-turbine. *Renew*

- 700 Energ 2020;146.
- 701 [22] Sotoudeh N, Maddahian R, Cervantes MJ. Investigation of Rotating Vortex Rope formation during load variation in a
702 Francis turbine draft tube. *Renew Energ* 2020;151:238-254.
- 703 [23] C AMAB, C BL, D WTS, C QZL, E MB, C JW, et al. Investigation on mutual traveling influences between the draft tube
704 and upstream components of a Francis turbine unit. *Renew Energ* 2020;162:973-992.
- 705 [24] Pasche S, Avellan F, Gallaire F. Optimal Control of Part Load Vortex Rope in Francis Turbines. *Journal of Fluids*
706 *Engineering* 2019.
- 707 [25] Alligne S, Nicolet C, Tsujimoto Y, Avellan F. Cavitation surge modelling in Francis turbine draft tube. *J Hydraul Res*
708 2014.
- 709 [26] Rezhghi A, Riasi A. Sensitivity analysis of transient flow of two parallel pump-turbines operating at runaway. *Renew*
710 *Energ* 2016;86:611-622.
- 711 [27] Kimleng K, Duan Y, Egusquiza M, Xu B, Egusquiza E. Transient analysis to air chamber and orifice surge tanks in a
712 hydroelectric generating system during the successive load rejection. *Energ Convers Manage* 2021;244.
- 713 [28] Chaudhry MH. Characteristics and Finite-Difference Methods. *Applied Hydraulic Transients* 2014;94:65-113.
- 714 [29] Xu B, Zhang J, Egusquiza M, Chen D, Li F, Behrens P, et al. A review of dynamic models and stability analysis for a
715 hydro-turbine governing system. *Renewable and Sustainable Energy Reviews* 2021;144:110880.
- 716 [30] A AR, A AR, B PT. Multi-objective optimization of hydraulic transient condition in a pump-turbine hydropower
717 considering the wicket-gates closing law and the surge tank position. *Renew Energ* 2020;148:478-491.
- 718 [31] Riasi A, Tazraei P. Numerical analysis of the hydraulic transient response in the presence of surge tanks and relief valves.
719 *Renew Energ* 2017;107:138-146.
- 720 [32] Hao RR. Influence study on the hydraulic transients of the equivalent diversion tunnel length. Tianjin University; 2010.
721 [In Chinese]
- 722 [33] Bookstein, F. L. Principal warps: thin-plate splines and the decomposition of deformations. *Pattern Analysis & Machine*
723 *Intelligence IEEE Transactions on* 1989.
- 724 [34] Novara D, McNabola A. A model for the extrapolation of the characteristic curves of Pumps as Turbines from a datum
725 Best Efficiency Point. *Energ Convers Manage* 2018;174:1-7.
- 726 [35] Alligne S, Nicolet C, Avellan F. Identification of Francis Turbine Helical Vortex Rope Excitation by CFD and Resonance
727 Simulation With the Hydraulic System. *American Society of Mechanical Engineers* 2011.
- 728 [36] Zhang L, Wu Q, Ma Z, Wang X. Transient vibration analysis of unit-plant structure for hydropower station in sudden
729 load increasing process. *Mech Syst Signal Pr* 2019;120:486-504.
- 730 [37] M Ssinger P, Jester-Zürker R, Jung A. Francis-99: Transient CFD simulation of load changes and turbine shutdown in a
731 model sized high-head Francis turbine. *Journal of Physics: Conference Series* 2017;782:12001.
- 732 [38] Norwegian Hydropower Center. Francis-99. <https://www.ntnu.edu/nvks/francis-99>. Accessed: 2016-09-15.
- 733 [39] Minakov AV, Platonov DV, Dekterev AA, Sentyabov AV, Zakharov AV. The analysis of unsteady flow structure and
734 low frequency pressure pulsations in the high-head Francis turbines. *Int J Heat Fluid Fl* 2015;53:183-194.
- 735 [40] Hong LC, Wang WY, Chen QJ. State Identification of Draft Tube Vortex Based on Continuous Wavelet Transform and
736 Convolutional Neural Network, *Guangdong electric power* 2018;31:1-6. [In Chinese]
- 737